



Article

# Self-Assembled BODIPY Derivative with A-D-A Structure as Organic Nanoparticles for Photodynamic/Photothermal Cancer Therapy

Guojing Li <sup>1</sup>, Mengqian Yang <sup>1</sup>, Qilong Sha <sup>1</sup>, Li Li <sup>1</sup>, Xiaogang Luo <sup>1,2</sup> and Fengshou Wu <sup>1,3,\*</sup>

<sup>1</sup> Hubei Key Laboratory of Novel Reactor and Green Chemical Technology, School of Chemical Engineering and Pharmacy, Wuhan Institute of Technology, Wuhan 430072, China

<sup>2</sup> School of Materials Science and Engineering, Zhengzhou University, Zhengzhou 450001, China

<sup>3</sup> Key Laboratory of Novel Biomass-Based Environmental and Energy Materials in Petroleum and Chemical Industry, Key Laboratory for Green Chemical Process of Ministry of Education, Wuhan Institute of Technology, Wuhan 430072, China

\* Correspondence: fswu@wit.edu.cn

**Abstract:** Organic nanomaterials have attracted considerable attention in the area of photodynamic and photothermal therapy, owing to their outstanding biocompatibility, potential biodegradability, well-defined chemical structure, and easy functionalization. However, it is still a challenge to develop a single organic molecule that obtains both photothermal and photodynamic effects. In this contribution, we synthesized a new boron-dipyrromethene (BODIPY)-based derivative (DPBDP) with an acceptor–donor–acceptor (A-D-A) structure by coupling 3,6-di(2-thienyl)-2,5-dihydropyrrolo [3,4-c] pyrrole-1,4-dione (DPP) and BODIPY. To enhance the hydrophilicity of the BODIPY derivative, the polyethylene glycol (PEG) chains were introduced to the *meso*- position of BODIPY core. The amphiphilic DPBDP was then self-assembled into related nanoparticles (DPBDP NPs) with improved hydrophilicity and enhanced absorbance in the NIR region. DPBDP NPs could simultaneously generate the singlet oxygen (<sup>1</sup>O<sub>2</sub>) and heat under the irradiation of a single laser (690 nm). The <sup>1</sup>O<sub>2</sub> quantum yield and photothermal conversion efficiency (PCE) of DPBDP NPs were calculated to be 14.2% and 26.1%, respectively. The biocompatibility and phototherapeutic effect of DPBDP NPs were evaluated through cell counting kit-8 (CCK-8) assay. Under irradiation of 690 nm laser (1.0 W/cm<sup>2</sup>), the half maximal inhibitory concentration (IC<sub>50</sub>) of DPBDP NPs was calculated to be 16.47 μg/mL. Thus, the as-prepared DPBDP NPs could be acted as excellent candidates for synergistic photodynamic/photothermal therapy.



**Citation:** Li, G.; Yang, M.; Sha, Q.; Li, L.; Luo, X.; Wu, F. Self-Assembled BODIPY Derivative with A-D-A Structure as Organic Nanoparticles for Photodynamic/Photothermal Cancer Therapy. *Int. J. Mol. Sci.* **2022**, *23*, 14473. <https://doi.org/10.3390/ijms232214473>

Academic Editor: Yury A. Skorik

Received: 12 August 2022

Accepted: 3 October 2022

Published: 21 November 2022

**Publisher's Note:** MDPI stays neutral with regard to jurisdictional claims in published maps and institutional affiliations.



**Copyright:** © 2022 by the authors. Licensee MDPI, Basel, Switzerland. This article is an open access article distributed under the terms and conditions of the Creative Commons Attribution (CC BY) license (<https://creativecommons.org/licenses/by/4.0/>).

**Keywords:** BODIPY; nanoparticles; self-assembly; photodynamic therapy; photothermal therapy

## 1. Introduction

Cancer is the main disease that threatens a human being's health [1]. The development of safe and effective treatments for cancer has received considerable attention nowadays [2–5]. Among the various cancer treatment strategies, phototherapy, including photodynamic therapy (PDT) and photothermal therapy (PTT), is a promising approach due to its safety, high efficiency, and non-invasiveness [6–8]. In PDT, the photosensitizer is irradiated by an appropriate wavelength of light to generate the reactive oxygen species (ROS), causing the death of tumor cells [9–11]. For PTT, the photothermal agent absorbs the laser energy to generate heat to thermally ablate the tumor [12,13]. The combination of PDT and PTT could enhance cancer therapy through the synergistic effect [14,15].

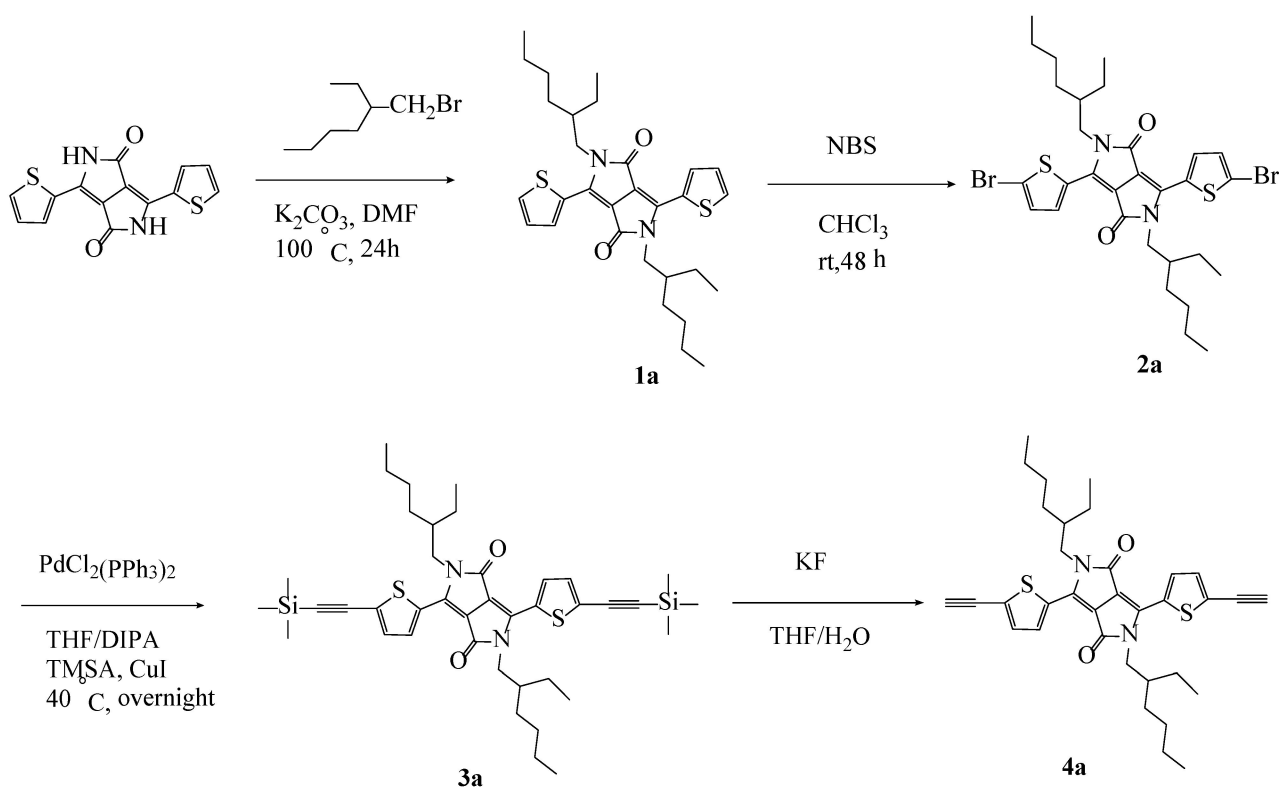
The chemical structure of the photosensitizers or photothermal agents plays an important role in the process of phototherapy, which directly affects its treatment efficacy. In the past few years, cyanine, rhodamines, and porphyrin derivatives have been widely used as photosensitizers in phototherapy [16–21]. Boron-dipyrromethene (BODIPY), bearing the

large conjugated structure, was demonstrated as a new type of near-infrared fluorescent dye and photosensitizer in recent years due to its eminent characteristics, such as high fluorescence quantum yield, large molar extinction coefficient, good photo-stability, and efficient ROS generation [22–24]. However, its poor water solubility and low absorption in the near-infrared region seriously limit its potential applications in biological area [25,26]. Therefore, the introduction of hydrophilic groups and conjugated bone in molecule are generally used to overcome these limits [27,28]. In this context, here we designed and synthesized a new BODIPY-based compound (DPBDP) with a typical acceptor–donor–acceptor (A-D-A) structure, where the diketopyrrolopyrrole (DPP) acted as the donor, with the boron-dipyrrromethene unit as the acceptor. The A-D-A structure in DPBDP could enhance the intramolecular charge transfer (ICT) and reduce the energy band gap, resulting in the redshift of the absorption to the near-infrared region. The covalent conjugation of 1, 8-naphthalenediimine (NDI) with BODIPY core can further promote the intramolecular charge transfer due to its strong electron withdrawing ability, and the PEG chains in NDI unit increase the hydrophilicity of the whole compound. Due to the amphiphilicity of DPBDP, it could self-assemble into the related nanoparticles (DPBDP NPs) by the reprecipitation method. DPBDP NPs exhibit high colloidal stability in aqueous solution with an average size of about 145 nm. Compared with the organic molecule, DPBDP NPs exhibit the red-shifted absorption with the maximum peak around 670 nm. In addition, DPBDP NPs can simultaneously generate  $^1\text{O}_2$  and heat under a single laser irradiation (690 nm). The low dark cytotoxicity and high photocytotoxicity of DPBDP NPs were investigated by the CCK-8 method and PI staining assay against the HeLa cells. Therefore, DPBDP NPs could be used as potential nanoagents in cancer phototherapy through a synergistic PDT/PTT treatment manner.

## 2. Results and Discussion

### 2.1. Synthesis

The synthetic routes of the intermediates and DPBDP NPs are shown in Schemes 1 and 2. In brief, Compound **1a** was synthesized by reacting DPP and 2-ethylhexyl bromide in DMF in the presence of  $\text{K}_2\text{CO}_3$ . Compound **4a** was synthesized via typical Sonogashira coupling. Compound **6b** was synthesized according to the previously reported method [29]. After iodization with N-iodosuccinimide (NIS) in  $\text{CHCl}_3$ , the monoiodized compound **7b** was obtained in high yield [30–32]. Finally, DPBDP was synthesized by the conjugation of compound **4a** with compound **7b** [33]. Because of the electron-donating characteristic of diketopyrrolopyrrole (DPP) and the electron-withdrawing ability of boron-dipyrrromethene, DPBDP exhibited a typical donor (D)–acceptor (A) structure, which could facilitate the intramolecular charge transfer, benefiting the  $\pi$ - $\pi$  stacking. Moreover, the hydrophilicity of PEG chain in boron-dipyrrromethene and the introduction of alkyl chains in DPP endow DPBDP with amphiphilic characteristic. The amphiphilic DPBDP could self-assemble into related nanoparticles (DPBDP NPs) through  $\pi$ - $\pi$  stacking and hydrophobic interaction without the addition of an extra polymer, as shown in Scheme 2.



**Scheme 1.** The synthetic routes of compound 4a.

## 2.2. Theoretical Calculation

The geometry optimizations of DPBDP were conducted through Avogadro soft. The density functional theory (DFT) calculations were investigated to obtain the electronic structures and transition energy of DPBDP with Gaussian 09 through B3LYP/sto-3g technique. As shown in Figure 1, the LUMO orbital was predominantly located on the BODIPY core, while the HOMO orbital was mainly located on the DPP unit. Accordingly, the electrons transfer from DPP to BODIPY structure would happen when DPBDP was excited to the excited states, further verifying the donor–acceptor structure of DPBDP. The HOMO energy level of DPBDP was calculated to be  $-7.2913\text{ eV}$ , while the LUMO energy levels was determined as  $-2.2251\text{ eV}$ . According to these values, the energy band gap of DPBDP was estimated as  $5.0662\text{ eV}$ .

## 2.3. Characterization

The morphology and particle size of DPBDP NPs were described through transmission electron microscopy (TEM) and dynamic light scattering (DLS). As shown in Figure 2A, DPBDP NPs exhibited the spherical morphology with the particle size of around  $140\text{ nm}$ . The DLS result revealed that DPBDP NPs had a reasonably uniform particle size distribution, with an average size of approximately  $145\text{ nm}$  (Figure 2B), beneficial for the passive tumor targeting due to the enhanced permeability and retention (EPR) effect. Besides, the zeta potential of DPBDP NPs was valued as  $-18.3\text{ mV}$  (Figure 2C), which facilitated the stability of nanoparticles in aqueous medium due to the electrostatic repulsion.



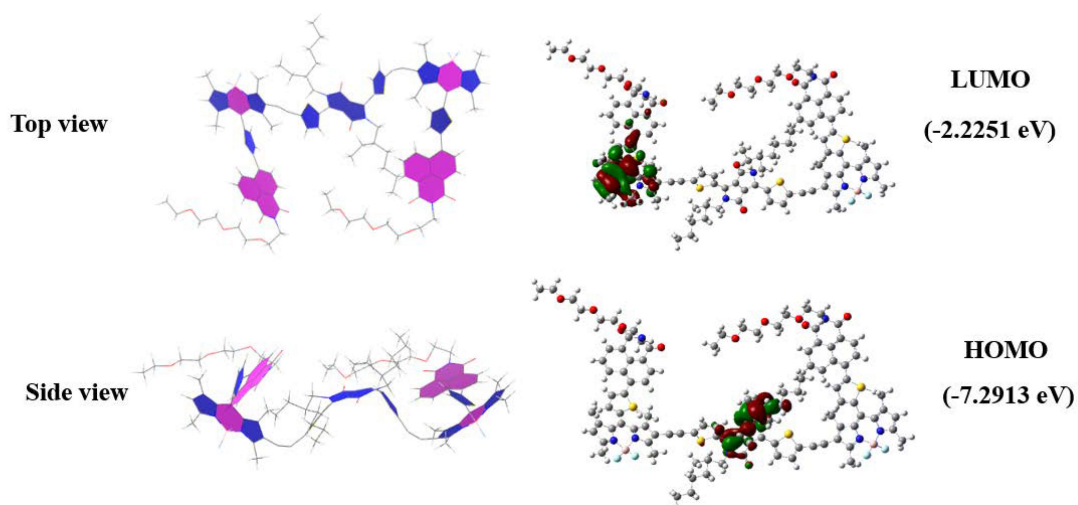


**Figure 1.** Optimized geometry and the frontier molecular orbitals electron density distribution of DPBDP.

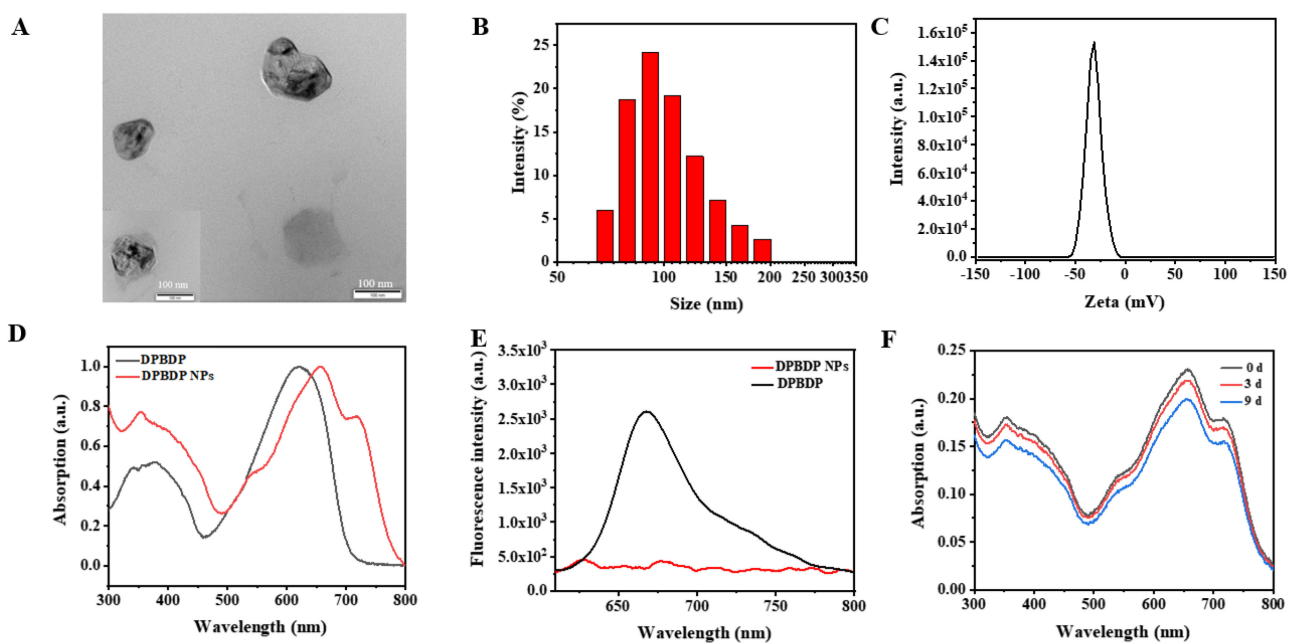


**Figure 2.** (A) The TEM image of DPBDP NPs, scale bar: 100 nm; (B) the DLS profile of DPBDP NPs; (C) the zeta potential of DPBDP NPs in DI water; (D) absorption spectra of DPBDP and DPBDP NPs; (E) fluorescence spectra of DPBDP, DPBDP NPs and ZnPc; (F) absorption spectra of DPBDP NPs in deionized water for several days.

#### 2.4. Photophysical Properties

The photophysical data of DPBDP and DPBDP NPs are summarized in Table 1.

**Table 1.** The photophysical properties of DPBDP and DPBDP NPs.

Sample	Absorption Peaks (nm)	$\epsilon$ (L·mol <sup>-1</sup> ·cm <sup>-1</sup> )	Emission Peaks (nm)	$\Phi_f^a$	$\Phi_\Delta^b$
DPBDP	621	$3.0 \times 10^5$	672	0.18	0.088
DPBDP NPs	653	$3.3 \times 10^5$	—	—	0.142

<sup>a</sup> The fluorescence quantum yields ( $\Phi_f$ ) were determined using zinc phthalocyanine as a reference [34,35]; <sup>b</sup> the singlet oxygen quantum yields ( $\Phi_\Delta$ ) were computed using 1,3-diphenylisobenzofuran (DPBF) as a capture reagent and methylene blue (MB) as a reference under 690 nm laser irradiation [36,37].

The UV-vis absorption spectrum of DPBDP and DPBDP NPs were examined in THF and DI water, respectively. As shown in Figure 2D, the absorption spectra of DPBDP and DPBDP NPs were similar in trend, with maximum peaks at 621 and 653 nm, respectively. Comparing with that of DPBDP, the absorption spectrum of DPBDP NPs broadened and red-shifted to some extent, probably due to the aggregation of molecules in the nanoparticles. The fluorescence spectrum of DPBDP and DPBDP NPs were investigated in the THF and aqueous solution, respectively. As shown in Figure 2E, DPBDP exhibited the strong red emission under excitation of 620 nm, with the maximum emission peak at 672 nm. However, after transforming into the nanoparticles, the fluorescence of molecule was significantly quenched, probably due to the aggregation-caused quenching (ACQ) phenomenon. The fluorescence quantum yield of DPBDP was valued to be 0.18 with ZnPc as a reference (Figure S1). The stability of DPBDP NPs in deionized water was assessed by UV-vis absorption spectrum. As shown in Figure 2F, the absorption spectrum of DPBDP NPs did not display any significant variation in a period of several days' storage, indicating their high stability in water.

### 2.5. Reactive Oxygen Species (ROS) Generation

The reactive oxygen species (ROS) generation of DPBDP and DPBDP NPs was determined using 2',7'-dichlorodihydrofluorescein diacetate (DCFH-DA) as a probe, which could be oxidized to green fluorescent DCF by ROS. As indicated in Figure 3A, the fluorescence intensity of the mixture solution of DCFH-DA and DPBDP NPs enhanced gradually with the irradiation (690 nm laser) time, which was significantly faster than that of DPBDP, indicating the higher ROS efficiency of DPBDP NPs. The singlet oxygen (<sup>1</sup>O<sub>2</sub>) generation ability of DPBDP and DPBDP NPs was further quantitatively evaluated through 1,3-diphenylisobenzofuran (DPBF) method with methyl blue as standard (Figure 3B). As shown in Figure S2, the <sup>1</sup>O<sub>2</sub> quantum yield of DPBDP NPs (0.142) was apparently higher than that of DPBDP (0.088), which agreed well with the result of the DCFH method.

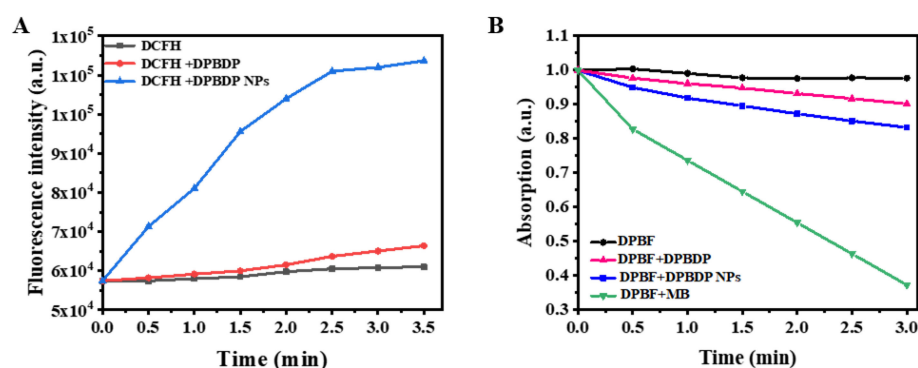


**Figure 3.** (A) Fluorescence intensity of DCF at 414 nm in the presence of DPBDP NPs as a function of illumination time; (B) linear degradation of DPBF solution with DPBDP and DPBDP NPs.

### 2.6. Photothermal Properties

The photothermal properties of DPBDP NPs were investigated by recording the temperature change of the solution at different concentrations and under laser irradiation

at different power densities. As indicated in Figure 4A, the temperature rise of solution was positively correlated with the concentration of DPBDP NPs under laser irradiation (690 nm, 1.5 W/cm<sup>2</sup>, 10 min). Furthermore, the temperature elevation of DPBDP NPs was dependent on the laser power density (Figure 4B). The temperature elevation of the aqueous solution at different concentration was visually verified by the thermal images of the corresponding solutions after laser irradiation for 10 min (Figure 4C). The photothermal conversion efficiency (PCE) of DPBDP NPs was measured by monitoring the temperatures change of DI water and DPBDP NPs under continuous irradiation for 10 min, followed by cooling for 10 min (Figure 4D). Based on the data obtained (Figures S3 and S4), the photothermal conversion efficiency (PCE) of DPBDP NPs was calculated to be 26.1%. Moreover, the temperature change of DPBDP NPs did not display any significant variation after five cycles of heating and cooling (Figure 4E), implying the favorable photothermal stability of DPBDP NPs. Therefore, DPBDP NPs could be employed as a prospective therapeutic agent for PTT.

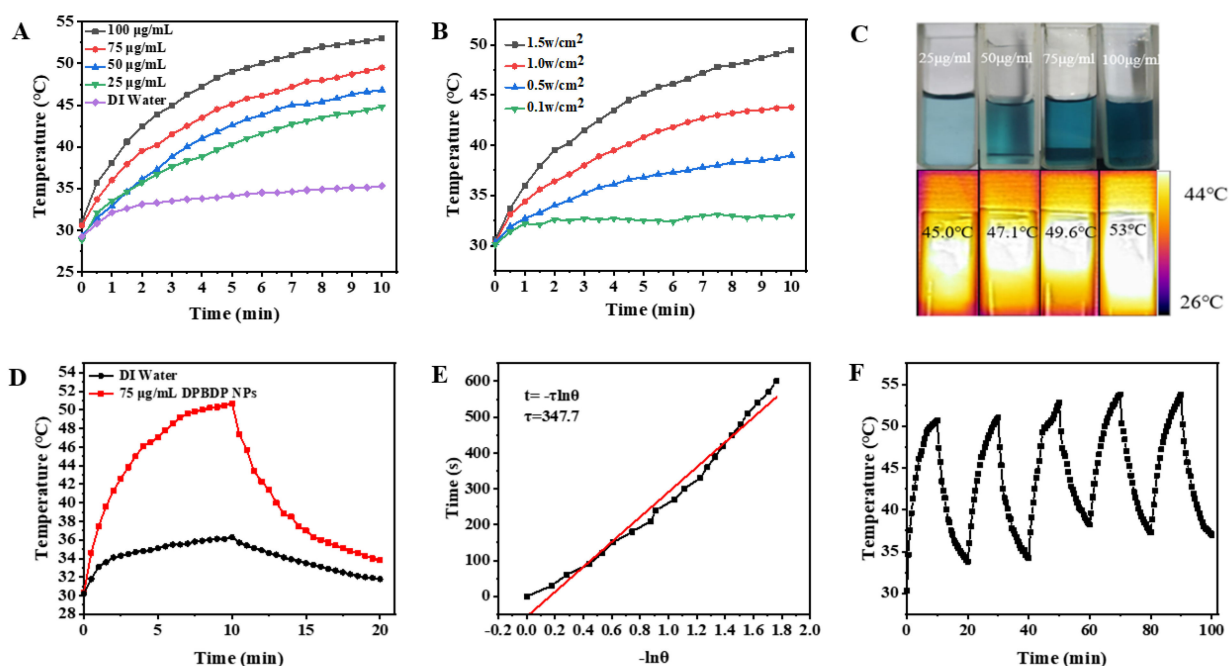


**Figure 4.** Photothermal properties of DPBDP NPs. (A) Photothermal curves of DPBDP NPs at several concentrations under 690 nm laser (1.5 W/cm<sup>2</sup>) irradiation; (B) photothermal curves of DPBDP NPs (75 µg/mL) under 690 nm laser irradiation at different laser power densities; (C) optical pictures and photothermal imaging of DPBDP NPs solution with different concentrations; (D) photothermal conversion effect of DPBDP NPs (75 µg/mL) and water under 690 nm irradiation; (E)  $-\ln\theta$  curve fitting of cooling time to temperature driving force in cooling phase of DPBDP NPs; (F) photothermal stability of DPBDP NPs during the five cycles of laser irradiation (75 µg/mL, 1.5 W/cm<sup>2</sup>).

### 2.7. Cell Viability Assay

The biocompatibility and phototherapeutic effect of DPBDP NPs were evaluated through CCK-8 assay. As shown in Figure 5A and Figure S5, after incubation with DPBDP NPs in dark for 24 h, the HeLa cells still maintained over 90% viability even at the concentration of 25 µg/mL, indicating the good biocompatibility of DPBDP NPs. In contrast, under 690 nm laser irradiation (1.0 W/cm<sup>2</sup>) for 10 min, the cell viability decreased with the concentration of DPBDP NPs. The survival rate of cancer cells was dropped to 18% when the concentration of DPBDP NPs was elevated to 25 µg/mL, suggesting their excellent phototherapeutic efficacy. The half maximal inhibitory concentration (IC<sub>50</sub>) of DPBDP NPs under 690 nm laser (1.0 W/cm<sup>2</sup>) irradiation was calculated to be 16.47 µg/mL.

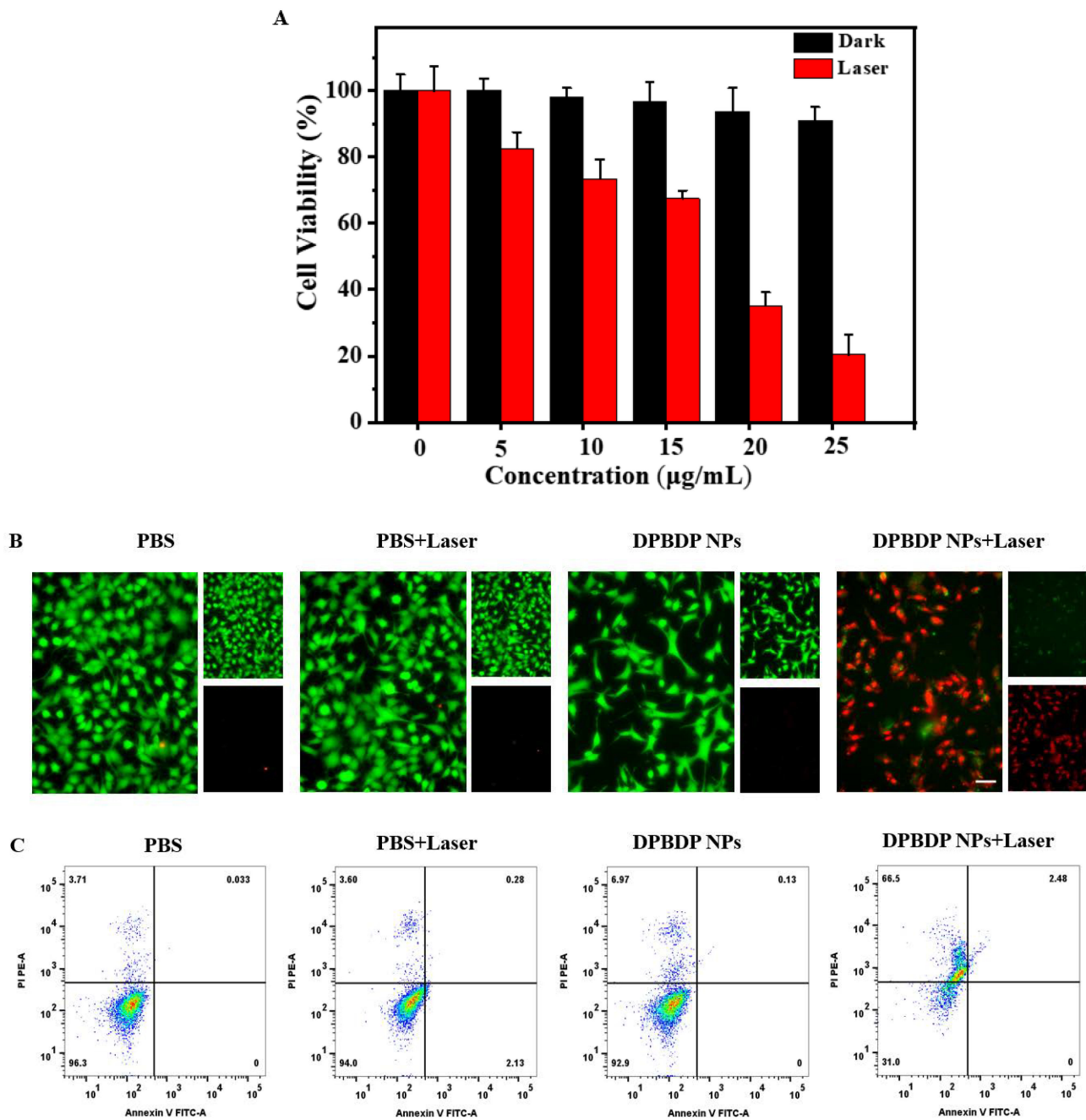


**Figure 5.** (A) CCK-8 assay of HeLa cells without or with 690 laser irradiation ( $1.0 \text{ W/cm}^2$ , 10 min); (B) calcein-AM and PI staining after 12 h incubation with PBS, PBS+laser, DPBDP NPs and DPBDP NPs+laser, scale bar =  $20 \mu\text{m}$ ; (C) cell apoptosis and necrosis level of HeLa cells stained by Annexin V-FITC/PI after 12 h incubation with PBS, PBS+laser, DPBDP NPs and DPBDP NPs+laser.

### 2.8. Live/Dead Cell Staining Assay

To further verify the biocompatibility and phototoxicity of DPBDP NPs, calcein-AM and PI staining was carried out, where the propidium iodide (PI) stains the dead cells with red color, while calcein-AM stains the living cells with green. As shown in Figure 5B, similar to the control groups (PBS and PBS+laser), the DPBDP NPs group did not display any significant red fluorescence, indicating the good biocompatibility of DPBDP NPs. However, the DPBDP NPs+laser group displayed clear red fluorescence and little green fluorescence, suggesting that the DPBDP NPs had a high phototherapeutic effect.

### 2.9. Apoptosis and Necrosis Assay

Meanwhile, the apoptosis level of HeLa cells in these groups was investigated by flow cytometer. As shown in Figure 5C, the apoptosis and necrosis percentage of cells in the DPBDP NPs+laser group was 69%, which was significantly higher than that of PBS group (3.7%), PBS+laser group (6%), and DPBDP NPs group (7.1%). Thus, DPBDP NPs presented the synergistic therapeutic effect (PTT/PDT) against HeLa cells, which was consistent with the result of the live/dead cell staining assay.

### 2.10. The Intracellular ROS Generation

The generation of ROS in cancer cells was investigated using 2',7'-dichlorofluorescein diacetate (DCFH-DA) as a probe [38,39], which could be transformed to fluorescent 2',7'-dichlorofluorescein (DCF) upon reacting with ROS produced by NPs under irradiation [40,41]. As shown in Figure 6, an intense green emission was observed around the nucleus of the HeLa cells, which was stained with Hoechst 33342 (blue fluorescence), suggesting the efficient intracellular ROS generation upon laser irradiation.

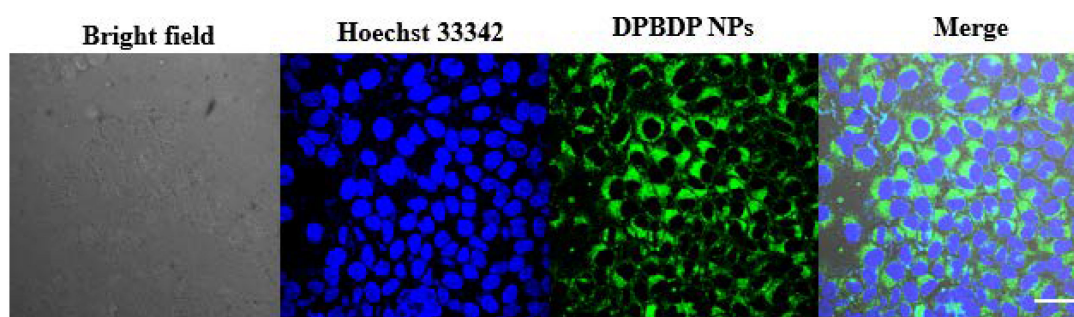


**Figure 6.** ROS generation in HeLa cells after incubation with DPBDP NPs (20  $\mu\text{g}/\text{mL}$ ) for 12 h followed by the treatment with DCFH-DA (10  $\mu\text{M}$ ) for 1 h and 690 nm laser irradiation (1.0  $\text{W}/\text{cm}^2$ , 5 min), scale bar = 20  $\mu\text{m}$ .

## 3. Experimental Sections

### 3.1. Materials and Characterization

All the starting chemicals were obtained from Aladdin (Shanghai, China) and used without further purification. The structures of intermediates and targeting materials were characterized by NMR spectra on the Agilent 400MR spectrometer, and mass spectra on a Bruker Auto flex MALDI-TOF mass spectrometer (Figures S6–S16). The absorption and fluorescence spectra were recorded through UV-vis Spectrophotometer (Shimadzu, Kyoto, Japan) and Fluorescence Spectrometer (PE LS55, Waltham, MA, USA), respectively. The DLS and zeta potential were measured by a Mavern ZetaSizer Nano-ZS (Mavern Instruments, Beijing, China). The TEM image was studied on the JEM-2100 transmission electron microscope. The excitation light was provided by a fiber-coupled 690 nm laser (MW-GX-690/700Mw, Changchun, China).

### 3.2. Synthesis of Compound 1a

To a solution of DPP (0.9 g, 4 mmol) and anhydrous potassium carbonate (2.07 g, 15 mmol) in 40 mL of N, N-dimethylformamide, brominated isooctane (2.3 g, 12 mmol) was injected under nitrogen atmosphere. After stirring at 100  $^{\circ}\text{C}$  for 24 h, the solvent was removed by rotary evaporator. The residue was purified by silica gel column chromatography (eluent: DCM: petroleum ether = 1:1) to obtain red solid compound **1a** (1.7 g, 53%).  $^1\text{H}$ NMR (400 MHz,  $\text{CDCl}_3$ )  $\delta$ : 8.87 (dd,  $J$  = 1.0 Hz, 3.9 Hz, 2H), 7.62 (dd,  $J$  = 1.1 Hz, 5.1 Hz, 2H), 7.26 (dd,  $J$  = 3.9 Hz, 5.0 Hz, 2H), 4.01 (d,  $J$  = 7.6 Hz, 4H), 1.90 (m, 2H), 1.22 (m, 8H), 0.87 (m, 12H).

### 3.3. Synthesis of Compound 2a

Compound **1a** (262 mg, 0.5 mmol) and NBS (214 mg, 1.2 mmol) were dissolved in anhydrous  $\text{CH}_2\text{Cl}_2$  (20 mL). After stirring at room temperature in dark for 48 h, the reaction mixture was washed with saturated solution of  $\text{Na}_2\text{SO}_3$ . The organic layer was collected, and the solvent was removed under reduced pressure. The residue was purified by silica gel column chromatography (eluent: DCM: MeOH = 120:1). Compound **2a** was isolated as a red solid (192 mg, 48%).  $^1\text{H}$  NMR (400 MHz,  $\text{CDCl}_3$ )  $\delta$  8.66 (d,  $J$  = 4.2 Hz, 2H), 7.24 (d,  $J$  = 4.2 Hz, 2H), 3.97–3.93 (m, 4H), 1.32 (dd,  $J$  = 13.6, 6.3 Hz, 18H), 0.90 (d,  $J$  = 7.9 Hz, 12H).

### 3.4. Synthesis of Compound 3a

Compound **2a** (0.100 g, 0.15 mmol), CuI (2.8 mg, 0.015 mmol),  $\text{PdCl}_2(\text{PPh}_3)_2$  (5 mg, 0.0073 mmol), THF (6 mL), triethylamine (4 mL), and trimethylsilylacetylene (0.1 mL, 0.7 mmol) were added to a 50 mL Schlenk flask under nitrogen atmosphere. After being heated to 50 °C overnight, the solvent was removed under vacuum, and the crude product was further purified by silica gel column chromatography using petroleum ether/DCM (2:1) as eluent. The product was isolated as a dark purple solid with a yield of 70%.  $^1\text{H}$  NMR (400 MHz,  $\text{CDCl}_3$ )  $\delta$  8.81 (d,  $J$  = 4.1 Hz, 2H), 7.32 (d,  $J$  = 4.1 Hz, 2H), 3.98 (dd,  $J$  = 7.7, 3.8 Hz, 4H), 1.30 (ddd,  $J$  = 21.1, 11.6, 6.6 Hz, 18H), 0.87 (d,  $J$  = 6.9 Hz, 12H), 0.27 (s, 18H).

### 3.5. Synthesis of Compound 4a

Compound **3a** (0.1 g, 0.14 mmol), KF (0.109 g, 1.89 mmol), and deoxygenated THF/water (9 mL/2.8 mL) were added to a two-neck flask. After stirring under nitrogen atmosphere overnight, the organic fraction was extracted with dichloromethane, and the organic layer was evaporated to obtain the crude mixture, which was then purified by silica gel column chromatography using DCM/petroleum ether (7:1) as an eluent. The product was obtained in 75% yield.  $^1\text{H}$  NMR (400 MHz,  $\text{CDCl}_3$ )  $\delta$  8.83 (d,  $J$  = 3.6 Hz, 2H), 7.38 (d,  $J$  = 3.5 Hz, 2H), 3.98 (s, 4H), 3.60 (s, 2H), 1.32–1.24 (m, 18H), 0.87 (d,  $J$  = 8.2 Hz, 12H).

### 3.6. Synthesis of Compound 4b

To a solution of ethanol (14 mL), 4-bromo-1,8-naphthalic anhydride (1.4 g, 5.1 mmol) and 2-(2-(2-methoxyethoxy) ethoxy) ethanamine **2** (1.08 g, 5.6 mmol) were added. After refluxing for 8 h, the solvent was removed under vacuum. The residue was dissolved in ethylacetate and washed with water. The organic extract was evaporated, and the crude product was purified by silica gel column chromatography (eluent: hexane: ethyl acetate = 5:1) to give compound **4b** as a yellow solid (2.92 g, 90%).  $^1\text{H}$  NMR (400 MHz,  $\text{CDCl}_3$ )  $\delta$  8.64 (dd,  $J$  = 7.3, 1.0 Hz, 1H), 8.55 (dd,  $J$  = 8.5, 1.0 Hz, 1H), 8.39 (d,  $J$  = 7.9 Hz, 1H), 8.03 (d,  $J$  = 7.9 Hz, 1H), 7.83 (dd,  $J$  = 8.4, 7.4 Hz, 1H), 4.42 (t,  $J$  = 6.1 Hz, 2H), 3.82 (t,  $J$  = 6.1 Hz, 2H), 3.69 (dd,  $J$  = 5.8, 3.6 Hz, 2H), 3.61 (dd,  $J$  = 5.9, 3.6 Hz, 2H), 3.57 (dd,  $J$  = 5.8, 3.8 Hz, 2H), 3.46 (dt,  $J$  = 14.1, 5.2 Hz, 4H), 1.16 (t,  $J$  = 7.0 Hz, 3H).

### 3.7. Synthesis of Compound 5b

Under the nitrogen atmosphere, compound **4b** (870 mg, 2 mmol), 2-aldehyde phenylboronic acid (374 mg, 2.4 mmol),  $\text{K}_2\text{CO}_3$  (1.1 g, 8 mmol) and  $\text{Pd}(\text{PPh}_3)_4$  (185 mg, 0.16 mmol) were dissolved in 12 mL mixed solution of THF and water (THF: water = 3:1). After refluxing for 12 h, the organic solvent was removed under vacuum, and the residue was purified by silica gel column chromatography (DCM:EA = 5:1) to give compound **5b** as a yellow solid (870 mg, 70%).  $^1\text{H}$  NMR (400 MHz,  $\text{CDCl}_3$ )  $\delta$  10.00 (s, 1H), 8.63 (dd,  $J$  = 14.4, 7.4 Hz, 2H), 8.51 (d,  $J$  = 8.5 Hz, 1H), 7.89 (d,  $J$  = 3.8 Hz, 1H), 7.84 (d,  $J$  = 7.6 Hz, 1H), 7.81–7.76 (m, 1H), 7.43 (d,  $J$  = 3.8 Hz, 1H), 4.44 (t,  $J$  = 6.1 Hz, 2H), 3.83 (t,  $J$  = 6.0 Hz, 2H), 3.71–3.68 (m, 2H), 3.63–3.60 (m, 2H), 3.57 (dd,  $J$  = 5.7, 3.9 Hz, 2H), 3.49–3.42 (m, 4H), 1.15 (t,  $J$  = 7.0 Hz, 3H).

### 3.8. Synthesis of Compound 6b

To a two-necked round bottom flask, compound **5b** (1 mmol), 2,4-dimethylpyrrole (2.5 mol), and anhydrous DCM (40 mL) were added under nitrogen atmosphere. After

stirring at room temperature for 30 min, TFA (10  $\mu$ L) was added dropwise. The resulting solution was then stirred for another 12 h followed by the addition of DDQ (1 mmol). After 2 h, 10 mL TEA was added to quench the reaction. Then, 10 mmol boron trifluoride ether was added, and the reaction mixture was stirred at room temperature for another 6 h. The solvent was then removed under vacuum, and the residue was purified by silica gel column chromatography (eluent: DCM:MeOH = 120:1) to obtain compound **6b** with a yield about 17%.  $^1\text{H}$  NMR (400 MHz,  $\text{CDCl}_3$ )  $\delta$  8.62 (d,  $J$  = 7.6 Hz, 3H), 7.86–7.79 (m, 2H), 7.38 (d,  $J$  = 3.5 Hz, 1H), 7.16 (d,  $J$  = 3.6 Hz, 1H), 4.47 (t,  $J$  = 6.1 Hz, 2H), 3.86 (t,  $J$  = 6.1 Hz, 2H), 3.73 (dd,  $J$  = 5.7, 3.7 Hz, 2H), 3.64 (dd,  $J$  = 5.9, 3.6 Hz, 2H), 3.60 (dd,  $J$  = 5.8, 3.9 Hz, 2H), 3.51–3.46 (m, 4H), 2.58 (s, 6H), 1.82 (s, 6H), 1.17 (t,  $J$  = 7.0 Hz, 3H).

### 3.9. Synthesis of Compound **7b**

Compound **6b** (200 mg, 0.31 mmol) and NIS (229 mg, 1.24 mmol) were dissolved in anhydrous  $\text{CH}_2\text{Cl}_2$  (15 mL). After stirring at room temperature for half an hour, the saturated solution of  $\text{Na}_2\text{SO}_3$  was added. The organic fraction was extracted with DCM, which was then concentrated under vacuum. The obtained residue was purified by silica gel column chromatography (eluent: DCM:MeOH = 120:1) to obtain compound **7b** as an orange solid (252 mg, 92%).  $^1\text{H}$  NMR (400 MHz,  $\text{CDCl}_3$ )  $\delta$  8.67–8.54 (m, 3H), 7.85–7.77 (m, 2H), 7.36 (dd,  $J$  = 6.3, 3.5 Hz, 1H), 7.14 (dd,  $J$  = 3.5, 1.2 Hz, 1H), 6.06 (s, 1H), 4.45 (t,  $J$  = 6.0 Hz, 2H), 3.83 (t,  $J$  = 6.0 Hz, 2H), 3.70 (dd,  $J$  = 5.7, 3.4 Hz, 2H), 3.60 (ddd,  $J$  = 9.5, 5.2, 3.1 Hz, 4H), 3.50–3.43 (m, 4H), 2.60 (d,  $J$  = 29.9 Hz, 6H), 1.80 (s, 6H), 1.15 (t,  $J$  = 7.0 Hz, 3H).

### 3.10. Synthesis of DPBDP

To a 25 mL flask, compound **4a** (30 mg, 0.051 mmol), **7b** (126 mg, 0.15 mmol),  $\text{AsPh}_3$  (200 mg, 0.523 mmol), bis-(triphenylphosphine) palladium dichloride (15 mg, 0.02 mmol), and cuprous iodide (3 mg, 0.015 mmol) were dissolved in 12 mL mixed solution of toluene and triethylamine (5:1). After stirring at 95  $^\circ\text{C}$  under argon overnight, the solvent was removed in vacuum. The obtained residue was purified through silica gel column chromatography (DCM:MeOH: 120:1) to yield a blue solid (17 mg, 15%).  $^1\text{H}$  NMR (400 MHz,  $\text{CDCl}_3$ )  $\delta$  8.96–8.82 (m, 2H), 8.69–8.54 (m, 4H), 7.97–7.67 (m, 5H), 7.53 (s, 1H), 7.40 (s, 1H), 7.29 (d,  $J$  = 4.0 Hz, 1H), 7.19 (s, 3H), 6.80 (d,  $J$  = 8.2 Hz, 1H), 6.15 (s, 1H), 5.34 (s, 1H), 4.48–3.43 (m, 28H), 2.65 (d,  $J$  = 37.1 Hz, 6H), 1.89 (d,  $J$  = 29.4 Hz, 6H), 1.65 (d,  $J$  = 30.0 Hz, 8H), 1.26 (d,  $J$  = 13.9 Hz, 26H), 1.16 (t,  $J$  = 7.0 Hz, 6H), 0.92–0.83 (m, 12H).  $^{13}\text{C}$  NMR (101 MHz,  $\text{CDCl}_3$ )  $\delta$  163.04 (s), 131.08 (d,  $J$  = 10.0 Hz), 128.89 (s), 128.01 (s), 127.51 (d,  $J$  = 12.2 Hz), 76.33 (s), 76.01 (s), 75.69 (s), 69.57 (s), 69.16 (s), 68.74 (s), 66.89 (s), 65.58 (s), 38.26 (s), 30.91 (s), 29.01 (s), 28.68 (s), 28.34 (s), 26.19 (s), 22.04 (s), 21.67 (s), 14.10 (s), 13.07 (d,  $J$  = 7.2 Hz), 11.86 (s), 9.47 (s). MALDI-TOF MS: calcd:1939.7345, found: 1939.7399.

### 3.11. Preparation of DPBDP Nanoparticles

DPBDP NPs were prepared through the reprecipitation approach. Specifically, DPBDP (1 mg/mL) in THF was added dropwise to DI water under sonication in a period of 15 min. The organic solvent was then removed by air blowing.

### 3.12. Photothermal Performances

The temperature of the DPBDP NPs solution at different concentrations was recorded under irradiation of a 690 nm laser (1.5  $\text{W}/\text{cm}^2$ , 10 min). Meanwhile, the solution temperature of DPBDP NPs (75  $\mu\text{g}/\text{mL}$ ) was measured upon 690 nm laser irradiation at different power densities. The PCE of DPBDP NPs was valued by comparing with DI water under irradiation of a 690 nm laser (1.5  $\text{W}/\text{cm}^2$ , 10 min) followed by cooling for 10 min.

### 3.13. Cells Culture and Cytotoxicity Assay

HeLa cells were cultured using Dulbecco's Modified Eagle's Medium (DMEM, Gibco, New South Wales, Australia) supplemented with 10% fetal bovine serum (FBS, Gibco, New South Wales, Australia) and 1% penicillin/streptomycin solution in a 37  $^\circ\text{C}$  cell incubator.

The cell viability was evaluated through CCK-8 assay. For the cell viability assay, HeLa cells were seeded in 96-well plates ( $1.0 \times 10^4$  cells per well) and incubated at 37 °C for 24 h. Subsequently, the cells were treated with different concentrations of DPBDP NPs (0, 5, 10, 15, 20 and 25 µg/mL) in medium. After incubation for another 12 h, the experimental cells were irradiated with or without 690 nm laser ( $1.0 \text{ W/cm}^2$ ) for 10 min. The cells were then incubated for another 12 h followed by washing with PBS buffer (pH 7.4). Finally, 10% CCK-8 solution was added to the above each well followed by the incubation for 1 h. The optical density (OD) at 450 nm was measured by a Spectra Max M5 microplate reader (Molecular Devices, San Francisco, CA, USA).

#### 3.14. Live/Dead Cell Staining Assay

HeLa cells were seeded in 96-well plates ( $3.0 \times 10^3$  cells per well) and incubated at 37 °C for 24 h. Thereafter, the previous medium was replaced by fresh medium with PBS or DPBDP NPs (20 µg/mL) for 24 h. Subsequently, the experimental wells were treated with or without a 690 nm laser irradiation ( $1.0 \text{ W/cm}^2$ , 10 min). After incubation for another 24 h, the cells were stained with calcein-AM and PI for 20 min, and the cellular state was observed using an inverted fluorescence microscope (Zeiss Axio Vert.A1, Jena, Germany).

#### 3.15. Apoptosis and Necrosis Assay

HeLa cells were seeded on 24-well plates ( $1.0 \times 10^5$  cells per well) and incubated at 37 °C for 24 h. Fresh medium with PBS or DPBDP NPs were added into the plates for 24 h incubation, followed by irradiation with or without 690 nm laser for 10 min. After 24 h, the cells were stained with an Annexin V-FITC/PI apoptosis detection kit. Finally, all the treated cells were harvested and analyzed by flow cytometer (FCM, BD FACSVerser, Piscataway, NJ, USA).

#### 3.16. The Intracellular ROS Generation

HeLa cells were plated into confocal dishes. After incubation for 24 h, the cells were co-incubated with DPBDP NPs (20 µg/mL). After 24 h, the medium was removed followed by washing twice with PBS. DCFH-DA (10 µM) in medium was then added. After incubation for 30 min, the cells were irradiated under 690 nm laser ( $1.0 \text{ W/cm}^2$ ) for 5 min, followed by washing twice with PBS. The cells were then stained with Hoechst 33342, and the fluorescent images were collected through a confocal laser scanning microscopy (Zeiss LSM780, Jena, Germany).

### 4. Conclusions

In summary, a new BODIPY-based derivative (DPBDP) with an acceptor–donor–acceptor (A-D-A) structure was synthesized by coupling the DPP unit with BODIPY core. To enhance the hydrophilicity of the BODIPY derivative, the PEG chains were introduced to the *meso*- position of BODIPY core. The amphiphilic DPBDP was then self-assembled into related nanoparticles (DPBDP NPs) with improved hydrophilicity and enhanced absorbance in the NIR region. Compared with the organic molecules, DPBDP NPs exhibited the red-shifted absorption with the maximum peak around 670 nm. DPBDP NPs exhibited efficient photodynamic and photothermal effects under irradiation of 690 nm laser. The  $^1\text{O}_2$  quantum yield and PCE of DPBDP NPs were calculated to be 14.2% and 26.1%, respectively. The good biocompatibility and remarkable phototoxicity of DPBDP NPs were verified through the CCK-8 method against HeLa cells. The  $\text{IC}_{50}$  of DPBDP NPs under irradiation was calculated to be 16.47 µg/mL. Therefore, DPBDP NPs could be used as potential nanoagents in cancer phototherapy through a synergistic PDT/PTT treatment manner.

**Supplementary Materials:** The following supporting information can be downloaded at: <https://www.mdpi.com/article/10.3390/ijms232214473/s1>

**Author Contributions:** Conceptualization, G.L. and M.Y.; methodology, Q.S. and L.L.; investigation, X.L.; supervision and project administration, F.W. All authors have read and agreed to the published version of the manuscript.

**Funding:** This work was supported by Key Project of Scientific Research Project of Hubei Provincial Department of Education (grant no. D20201504), the Opening Project of Hubei Key Laboratory of Novel Reactor and Green Chemical Technology (grant no. NRG202103), Outstanding Young and Middle-aged Scientific Innovation Team of Colleges and Universities of Hubei Province: “Biomass chemical technologies and materials” (grant no. T201908), and the Innovation Project of Key Laboratory of Novel Biomass-Based Environmental and Energy Materials in Petroleum and Chemical Industry (grant no. 2022BEEA06).

**Conflicts of Interest:** The authors declare no conflict of interest.

## References

1. Sung, H.; Ferlay, J.; Siegel, R.L.; Laversanne, M.; Soerjomataram, I.; Jemal, A.; Bray, F. Global Cancer Statistics 2020: GLOBOCAN Estimates of Incidence and Mortality Worldwide for 36 Cancers in 185 Countries. *CA Cancer J. Clin.* **2021**, *71*, 209–249. [[CrossRef](#)] [[PubMed](#)]
2. Mirza, F.N.; Khatri, K.A. The use of lasers in the treatment of skin cancer: A review. *J. Cosmet. Laser Ther.* **2017**, *19*, 451–458. [[CrossRef](#)] [[PubMed](#)]
3. Li, H.; Yue, L.; Wu, M.; Wu, F. Self-assembly of methylene violet-conjugated perylene diimide with photodynamic/photothermal properties for DNA photocleavage and cancer treatment. *Colloids Surf. B Biointerfaces* **2020**, *196*, 111351. [[CrossRef](#)] [[PubMed](#)]
4. Naud, C.; Thébault, C.; Carrière, M.; Hou, Y.; Morel, R.; Berger, F.; Diény, B.; Joisten, H. Cancer treatment by magneto-mechanical effect of particles, a review. *Nanoscale Adv.* **2020**, *2*, 3632–3655. [[CrossRef](#)] [[PubMed](#)]
5. Zheng, Y.; Gao, Y. Molecular targeted nanotheranostics for future individualized cancer treatment. *Expert Opin. Drug Deliv.* **2020**, *17*, 1059–1062. [[CrossRef](#)] [[PubMed](#)]
6. Wu, Q.; Zhu, Y.; Fang, X.; Hao, X.; Jiao, L.; Hao, E.; Zhang, W. Conjugated BODIPY Oligomers with Controllable Near-Infrared Absorptions as Promising Phototheranostic Agents through Excited-State Intramolecular Rotations. *ACS Appl. Mater. Interfaces* **2020**, *12*, 47208–47219. [[CrossRef](#)]
7. Yao, S.; Chen, L.; Jia, F.; Sun, X.; Su, H.; Liu, H.; Yang, L.; Wang, Z.; Wu, F.; Wang, K. Platinated porphyrin tailed with folic acid conjugate for cell-targeted photodynamic activity. *J. Lumin.* **2019**, *214*, 116552. [[CrossRef](#)]
8. Yang, M.; Deng, J.; Guo, D.; Sun, Q.; Wang, Z.; Wang, K.; Wu, F. Mitochondria-targeting Pt/Mn porphyrins as efficient photosensitizers for magnetic resonance imaging and photodynamic therapy. *Dye. Pigment.* **2019**, *166*, 189–195. [[CrossRef](#)]
9. Abrahamse, H.; Hamblin, M.R. New photosensitizers for photodynamic therapy. *Biochem. J.* **2016**, *473*, 347–364. [[CrossRef](#)]
10. Zhu, X.; Feng, W.; Chang, J.; Tan, Y.W.; Li, J.; Chen, M.; Sun, Y.; Li, F. Temperature-feedback upconversion nanocomposite for accurate photothermal therapy at facile temperature. *Nat. Commun.* **2016**, *7*, 10437. [[CrossRef](#)]
11. Li, X.; Lee, D.; Huang, J.D.; Yoon, J. Phthalocyanine-Assembled Nanodots as Photosensitizers for Highly Efficient Type I Photoreactions in Photodynamic Therapy. *Angew. Chem. Int. Ed. Engl.* **2018**, *57*, 9885–9890. [[CrossRef](#)] [[PubMed](#)]
12. Wu, F.; Yue, L.; Cheng, K.; Chen, J.; Wong, K.-L.; Wong, W.-K.; Zhu, X. Facile Preparation of Phthalocyanine-Based Nanodots for Photoacoustic Imaging and Photothermal Cancer Therapy In Vivo. *ACS Biomater. Sci. Eng.* **2020**, *6*, 5230–5239. [[CrossRef](#)] [[PubMed](#)]
13. Wang, Y.; Zhang, D.; Wang, J.; Xi, D.; Xu, Z.; Jiang, X.-D.; Du, J. Near-infrared vinyl-containing aza-BODIPY nanoparticles as photosensitizer for phototherapy. *Dye. Pigment.* **2022**, *198*, 110026. [[CrossRef](#)]
14. Shao, W.; Yang, C.; Li, F.; Wu, J.; Wang, N.; Ding, Q.; Gao, J.; Ling, D. Molecular Design of Conjugated Small Molecule Nanoparticles for Synergistically Enhanced PTT/PDT. *Nanomicro Lett.* **2020**, *12*, 147. [[CrossRef](#)] [[PubMed](#)]
15. Gao, F.; Sun, Z.; Zhao, L.; Chen, F.; Stenzel, M.; Wang, F.; Li, H.; Zhang, L.; Jiang, Y. Bioactive engineered photothermal nanomaterials: From theoretical understanding to cutting-edge application strategies in anti-cancer therapy. *Mater. Chem. Front.* **2021**, *5*, 5257–5297. [[CrossRef](#)]
16. Wu, F.; Yang, M.; Zhang, J.; Zhu, S.; Shi, M.; Wang, K. Metalloporphyrin-indomethacin conjugates as new photosensitizers for photodynamic therapy. *J. Biol. Inorg. Chem.* **2019**, *24*, 53–60. [[CrossRef](#)] [[PubMed](#)]
17. Deng, J.; Li, H.; Yang, M.; Wu, F. Palladium porphyrin complexes for photodynamic cancer therapy: Effect of porphyrin units and metal. *Photochem. Photobiol. Sci.* **2020**, *19*, 905–912. [[CrossRef](#)]
18. Lange, N.; Szlasa, W.; Saczko, J.; Chwilkowska, A. Potential of Cyanine Derived Dyes in Photodynamic Therapy. *Pharmaceutics* **2021**, *13*, 818. [[CrossRef](#)]
19. Chambi-Rocha, A.; Cabrera-Dominguez, M.E.; Dominguez-Reyes, A. Breathing mode influence on craniofacial development and head posture. *J. Pediatr. (Rio J.)* **2018**, *94*, 123–130. [[CrossRef](#)]

20. Wei, Y.; Hu, X.; Shen, L.; Jin, B.; Liu, X.; Tan, W.; Shangguan, D. Dicyanomethylene Substituted Benzothiazole Squaraines: The Efficiency of Photodynamic Therapy In Vitro and In Vivo. *EBioMedicine* **2017**, *23*, 25–33. [[CrossRef](#)]
21. Allison, R.R.; Sibata, C.H. Oncologic photodynamic therapy photosensitizers: A clinical review. *Photodiagnosis Photodyn. Ther.* **2010**, *7*, 61–75. [[CrossRef](#)]
22. Burgess, A.L.a.K. BODIPY Dyes and Their Derivatives: Syntheses and Spectroscopic Properties. *Chem. Rev.* **2007**, *107*, 4891–4932.
23. Kamkaew, A.; Lim, S.H.; Lee, H.B.; Kiew, L.V.; Chung, L.Y.; Burgess, K. BODIPY dyes in photodynamic therapy. *Chem. Soc. Rev.* **2013**, *42*, 77–88. [[CrossRef](#)] [[PubMed](#)]
24. Lu, H.; Mack, J.; Yang, Y.; Shen, Z. Structural modification strategies for the rational design of red/NIR region BODIPYs. *Chem. Soc. Rev.* **2014**, *43*, 4778–4823. [[CrossRef](#)]
25. Weissleder, R. A clearer vision for in vivo imaging. *Nat. Biotechnol.* **2001**, *19*, 316–317. [[CrossRef](#)]
26. Niu, S.L.; Massif, C.; Ulrich, G.; Renard, P.Y.; Romieu, A.; Ziessel, R. Water-soluble red-emitting distyryl-borondipyrromethene (BODIPY) dyes for biolabeling. *Chemistry* **2012**, *18*, 7229–7242. [[CrossRef](#)]
27. Ruijie, S.; Guomin, S.; Yanxin, L.; Ning, W.; Chencheng, F.; Xu, J.; Yanhui, L.; Chengzhi, G.; Yaqing, F.; Shuxian, M. Unique PDT and PTT synergistic effect between TPE and BODIPY. *Chem. Commun.* **2021**, *57*, 10035–10038. [[CrossRef](#)] [[PubMed](#)]
28. Zhao, M.; Xie, M.; Guo, J.; Feng, W.; Xu, Y.; Liu, X.; Liu, S.; Zhao, Q. Facile Phototherapeutic Nanoplatfrom by Integrating a Multifunctional Polymer and MnO<sub>2</sub> for Enhancing Tumor Synergistic Therapy. *Adv. Healthc. Mater.* **2019**, *8*, e1900414. [[CrossRef](#)] [[PubMed](#)]
29. Deng, J.; Yang, M.; Li, C.; Liu, G.; Sun, Q.; Luo, X.; Wu, F. Single molecular-based nanoparticles with aggregation-induced emission characteristics for fluorescence imaging and efficient cancer phototherapy. *Dye. Pigment.* **2021**, *187*, 109130. [[CrossRef](#)]
30. Collado, D.; Remon, P.; Vida, Y.; Najera, F.; Sen, P.; Pischel, U.; Perez-Inestrosa, E. Energy transfer in aminonaphthalimide-borondipyrromethene (BODIPY) dyads upon one- and two-photon excitation: Applications for cellular imaging. *Chem. Asian J.* **2014**, *9*, 797–804. [[CrossRef](#)] [[PubMed](#)]
31. Lima, C.F.R.A.C.; Rodriguez-Borges, J.E.; Santos, L.M.N.B.F. Exploring the selectivity of the Suzuki–Miyaura cross-coupling reaction in the synthesis of aryl naphthalenes. *Tetrahedron* **2011**, *67*, 689–697. [[CrossRef](#)]
32. Hussain, M.; El-Zohry, A.M.; Gobeze, H.B.; Zhao, J.; D’Souza, F.; Mohammed, O.F. Intramolecular Energy and Electron Transfers in Bodipy Naphthalenediimide Triads. *J. Phys. Chem. A* **2018**, *122*, 6081–6088. [[CrossRef](#)]
33. Singh, S.; Chithiravel, S.; Krishnamoorthy, K. Copolymers Comprising Monomers with Various Dipoles and Quadrupole as Active Material in Organic Field Effect Transistors. *J. Phys. Chem. C* **2016**, *120*, 26199–26205. [[CrossRef](#)]
34. Xu, Y.; Zhao, M.; Zou, L.; Wu, L.; Xie, M.; Yang, T.; Liu, S.; Huang, W.; Zhao, Q. Highly Stable and Multifunctional Aza-BODIPY-Based Phototherapeutic Agent for Anticancer Treatment. *ACS Appl. Mater. Interfaces* **2018**, *10*, 44324–44335. [[CrossRef](#)]
35. Morgan, J.; Yun, Y.J.; Aytou, A.J. Estimation of Singlet Oxygen Quantum Yield Using Novel Green-Absorbing Baird-type Aromatic Photosensitizers (dagger). *Photochem. Photobiol.* **2021**, *98*, 57–61. [[CrossRef](#)]
36. Mirenda, M.; Strassert, C.A.; Dico, L.E.; San Roman, E. Dye-polyelectrolyte layer-by-layer self-assembled materials: Molecular aggregation, structural stability, and singlet oxygen photogeneration. *ACS Appl. Mater. Interfaces* **2010**, *2*, 1556–1560. [[CrossRef](#)] [[PubMed](#)]
37. Shinji, K.; Chikama, T.; Okazaki, S.; Uto, Y.; Sueoka, K.; Pertiwi, Y.D.; Ko, J.A.; Kiuchi, Y.; Sakaguchi, T. Molecular characteristics of the photosensitizer TONS504: Comparison of its singlet oxygen quantum yields and photodynamic antimicrobial effect with those of methylene blue. *J. Photochem. Photobiol. B* **2021**, *221*, 112239. [[CrossRef](#)] [[PubMed](#)]
38. Usui, Y. Determination of quantum yield of singlet oxygen formation by photosensitization. *Chem. Lett.* **1973**, *2*, 743–744. [[CrossRef](#)]
39. Nosaka, Y.; Nosaka, A.Y. Generation and Detection of Reactive Oxygen Species in Photocatalysis. *Chem. Rev.* **2017**, *117*, 11302–11336. [[CrossRef](#)]
40. Zhang, Y.; Dai, M.; Yuan, Z. Methods for the detection of reactive oxygen species. *Anal. Methods* **2018**, *10*, 4625–4638. [[CrossRef](#)]
41. Luo, Z.; Liu, J.; Zhao, Q.; Xi, Y.; Peng, R.; Liao, J.; Diwu, Z. Detection of Reactive Oxygen Species in Live Cell Mitochondria. *Biophys. J.* **2017**, *112*, 132a. [[CrossRef](#)]